# Rewritable nano print of ionic liquids utilizing focused ion beam induced film wetting

**Hao Wang**

wanghpku@pku.edu.cn

Peking University

**Haohao Gu**

Peking University https://orcid.org/0009-0002-1209-5572

**Kaixin Meng**

Peking University

**Ruowei Yuan**

Peking University

**Siyang Xiao**

Boston University

**Yuying Shan**

Peking University

**Rui Zhu**

Peking University https://orcid.org/0000-0002-4396-7292

**Yajun Deng**

Shenzhen Technology University

**Xiaojin Luo**

Peking University

**Ruijie Li**

Peking University

**Lei Liu**

Peking University https://orcid.org/0000-0002-7226-8423

**Xu Chen**

North China Electric Power University

**Chuanhua Duan**

Boston University https://orcid.org/0000-0002-5453-5321

**Yuping Shi**

Peking University

---

**Article**

**Keywords:**

**Posted Date:** August 1st, 2023

**DOI:** https://doi.org/10.21203/rs.3.rs-3158562/v1



**Additional Declarations:** There is **NO** Competing Interest.

---

**Version of Record:** A version of this preprint was published at Nature Communications on April 5th, 2024. See the published version at https://doi.org/10.1038/s41467-024-47018-9.

# Title: Rewritable nano print of ionic liquids utilizing focused ion beam induced film wetting

**Authors:** Haohao Gu[1]†, Kaixin Meng[1]†, Ruowei Yuan[1], Siyang Xiao[3], Yuying Shan[1], Rui Zhu[2], Yajun Deng[6], Xiaojin Luo[4], Ruijie Li[4], Lei Liu[4], Xu Chen[5], Yuping Shi[4], Xiaodong Wang[5], Chuanhua Duan[3], Hao Wang[1*]

**Affiliations:**

[1] Laboratory of Heat and Mass Transport at Micro-Nano Scale, College of Engineering, Peking University; Beijing, 100871, P. R. China.

[2] School of Physics, Peking University; Beijing, 100871, P. R. China.

[3] Department of Mechanical Engineering, Boston University; Boston, 02155, Massachusetts, USA.

[4] School of Materials Science and Engineering, Peking University; Beijing 100871, P. R. China.

[5] Research Center of Engineering Thermophysics, North China Electric Power University; Beijing 102206, P. R. China.

[6] Julong College, Shenzhen Technology University; Shenzhen 518118, P. R. China.

*Corresponding author. Email: wanghpku@pku.edu.cn

†These authors contributed equally: Kaixin Meng, Haohao Gu.

**Abstract:**

Manipulating liquid flow over open solid substrate at nanoscale is important for printing, sensing, and energy devices. The predominant methods of liquid maneuvering usually involve complicated surface fabrications, while recent attempts employing external stimuli face difficulties in attaining nanoscale flow control. Here we report a largely unexplored ion beam induced film wetting (IBFW) technology for open surface nanofluidics. Local electrostatic forces, which are generated by the unique charging effect of Helium focused ion beam (HFIB), induce precursor film of ionic liquids and the disjoining pressure propels and stabilizes the nanofilm with desired patterns. The IBFW technique eliminates the complicated surface fabrication procedures to achieve nanoscale flow control, and enables the manufacturing of complex liquid circuit in a controllable and rewritable manner.

**Main Text:**

## Introduction

Programmable control of fluid motion over open solid surfaces at small scales[1,2] are crucial for countless technological applications such as printing[3,4], biosensing[5,6], energy generating[7,8], air water harvesting[9], and chemical synthesis[10] *etc*. The predominant methods resort to either topographical or chemical gradients fabricated on solid surfaces, such as micro(nano)channels[11,12], bioinspired surface structures[13–19], chemical modifications[20,21], *etc.* However, such methods permanently alter the solid substrate. Once fabrication finished, the flow pattern can barely be changed. Moreover, the cost of flow control increases significantly with the complexity of surface modifications. To improve the controllability and flexibility, external-field-stimuli have been recently adopted including temperature[22,23], light [24,25], magnetic[26,27] or electric fields[4,28,29]. The current external-field-stimuli methods mainly resort to the field induced surface-tension-gradients (STGs), which works well for system size below the capillary length ($\lambda_{capillary} \sim \sqrt{\gamma/\rho g} \sim 10^{-3}\ m$) since the surface energy dominates the free energy of micrometer systems. However, the spatial resolutions of such methods are restricted at microscale and fail to achieve nanoscale flow control. For instances, the reported thermal capillary films[23–25] have thickness above $5\ \mu m$ and minimum line width about $30\ \mu m$. More importantly, the finger instability is usually inevitable[30] in STG based methods and jeopardizes the patterning performances.

Actually, when the liquid film thickness approaches nanometer scale, the interfacial overlapping dominates the system free energy[31–33] instead of surface tension. Such phenomenon usually called disjoining pressure has been proved to be capable of stabilizing liquid nanofilm[34–36]. Therefore, to achieve patterning flow at nanoscale, the liquid film thickness needs to reach nanometer to harness the disjoining pressure to stabilize the film pattern, and also requires the spatial resolution of external-field-stimuli to attain nanometer size. Compared with thermal[25] and pyroelectrical[26,37] fields, electron/ion beams which can be readily focused to sub-nanometer size[38,39] emerge as a promising option of external-field-stimulus. For example, 120 keV electron beam has been reported to induce the stick-slip motion of water nanodroplets[39]. However, the flow speeds were slow (around $3 \sim 20\ nm/s$), the travel lengths were short (around $189\ nm$), and more importantly, the flow directions and trajectories were uncontrollable while the physical mechanism remained ambiguous. Despite of these, their results still revealed that the interaction between electron/ion beams and liquid is a prospective candidate for liquid maneuvering and can be harnessed for open surface nanofluidics.

Here, we present an unexplored concept of open surface nanofluidics called ion beam induced film wetting (IBFW) and achieve the nanoscale patterning of ionic liquids film without resorting to any surface fabrications or special electric circuits. The Helium focused ion beam (HFIB) is generated by a state-of-the-art Helium ion microscope[38] (HIM, ORION NanoFab, Zeiss), which can provide a beam spot of diameter $0.5\ nm$, and a wide range of dose densities. Since the HIM only operates in an ultra-high vacuum, we select ionic liquids (ILs) as the liquid material due to its ultra-low vapor pressure. Besides, ILs are versatile materials that play vital roles in biodegradable and biocompatible chemistry[40,41], propellants for aeronautics[42], and fabrication of electric double layer transistors[43]. We investigate the interaction between the HFIB and IL under different dose densities and discover an unreported liquid inducing mode of HFIB. The liquid inducing mode is attributed to electrical field induced ion emission and disjoining pressure which propels and stabilizes the liquid film pattern. Based on the IBFW inducing mode, we develop a

nano-printing technique of ILs, with film thickness down to $20\sim30\ nm$, minimal line width about $100\ nm$ and corner radius down to $20\ nm$, and compare its performances with the reported methods. We further demonstrate the potential of IBFW technique in the gas sensing field. The simplicity of IBFW technique suggests prospect in a range of liquid manipulation applications, such as smart manufacture of liquid circuit, nano-transistors fabrication[43] and biochemical sensing circuit printing. We expect this technique can open a new avenue for applications in nano-printing and nano-circuit manufacturing.

## Results and Discussions

### Working Procedures of IBFW

The experimental system consists of a solid substrate, liquid reservoir and the HIM. A clean PECVD $SiO_2$ wafer serves as the solid substrate and forms the base of liquid reservoir. A small droplet of 1-Ethyl-3-methylimidazolium Dicyanamide ([EMIM][DCA]) IL deposited on the substrate forms the liquid reservoir. The HIM provides the non-contact external stimulus, HFIB. We systematically investigate the interaction between HFIB and the IL employing different combinations of dwell time, $\tau$, and scan spot pixel spacing, $s$ (Fig. 1A). When dose density $D = I \cdot \tau \cdot s^{-2} < 2.5\ ions \cdot nm^{-2}$, the HFIB exerts negligible influence on both solid and liquid samples which is the imaging mode of HIM. At extremely high dose density ($D > 500\ ions \cdot nm^{-2}$), the HFIB decomposes/etches the samples and Helium bubbling may occur (Supplementary Fig. S1). However, at moderate dose density range ($2.5\ ions \cdot nm^{-2} \leq D < 200\ ions \cdot nm^{-2}$), the ILs are induced to flow into the irradiated area while the solid substrates remain intact (Supplementary Note S1) which is the liquid inducing mode of HIM. After the HFIB with appropriate parameters (Supplementary Table S1) scans outwards from the contact line (CTL) of reservoir (Fig. 1B), IL flow through local protrusions of CTL and branch off to form hierarchical rivulets (Supplementary Fig. S2, Video S1-4). The liquid inducing mode of HIM has not been reported to the best of our knowledge, and can be harnessed to develop a nano-printing technique.

As an example of IBFW printing technology (Fig. 1C,D), we induce small amount of liquid from the reservoir to fabricate a rectangular film pattern ($50\mu m \times 1\mu m$).

*Step1: Sample preparation.* A $SiO_2$ wafer is placed horizontally as the substrate, Fig. 1C. No surface fabrication or physical mask is needed. A 0.1 μL droplet of IL is deposited on substrate as the reservoir. The contact angle of the IL on the substrate is approximately 60° (Supplementary Fig. S3). Then the sample is transferred into the chamber of HIM.

*Step 2: CTL identification and pattern design.* Under the imaging mode of the HIM, the CTL of the droplet is identified. As the yellow dotted box marked in Fig. 1C, part of the CTL is chosen as the starting position of the film pattern (50 μm × 1 μm) which is drawn employing software Nano Patterning and Visualization Engine (NPVE). The NPVE rasterize-fills the pattern with scan spot arrays (Supplementary Fig. S4).

*Step 3: HFIB irradiation and liquid inducing.* Employing inducing mode of the HIM, the HFIB scans the designed area. The ion beam vector-scans the spot arrays point by point with serpentine scan style and specific beam parameters. Noteworthily, the starting position of scan should be located at or stuck into the CTL, and the scan direction should be outwards from the reservoir, while other configurations cannot achieve the best inducing performance (Supplementary Fig. S5) also the flood gun should be turned on. When the point-by-point irradiation finishes, the thin liquid film is fabricated with designed pattern (Fig. 1D).

As shown in Fig. 1D, IBFW fabricated nanofilm reproduces not only the size of the designed pattern (50 μm×1 μm), but also the straight edges and the 90° corners. Moreover, liquid film networks can be easily rewritten on the same solid substrate after the liquid is dissolved by acetone. As a result, the liquid film pathways can be reprogrammed in an on-demand manner as shown in Supplementary Fig. S6.

To further demonstrate the prospect in complex patterning of IBFW, we fabricate a liquid film pattern making up the words "PKU COE" (Peking University College of Engineering) in Fig. 1E. The word patterns are all drawn employing NPVE without physical masks. Throughout the patterning process, the liquid is induced to flow along arbitrary geometrical tracks with curved lanes, crisscross junctions, and corners to form complicated liquid networks. The liquid film well reproduces the designed pattern. The width and corner radius of the liquid film barely change during the propagation regardless of the complexity of the pattern. The inset of Fig. 1E presents an example of minimal line width, $100\ nm$, IBFW can achieve.

**Working Principles of IBFW**

When HFIB turned on, the Helium ions generate special charges distribution[44] in the $SiO_2$ substrate, the negative surface charges induce the primary ion emission from the IL reservoir (Fig.2A). Helium ions tend to penetrate sample and induce less damaging (Supplementary Fig. S7) [45]. Consequently, the positive charges (ions, holes) distribute deeply into the solids and are constrained within tens of nm in the lateral direction, and would be blocked by the anions in the IL reservoir. The electrons excited by incident ions attempt to escape from the substrate, but attracted by the positive charges that penetrate deeply. Hence the negative charges are trapped near the surface with wider lateral distribution and gather beyond the CTL region induce the cation emission from the reservoir. The flood gun experiments prove that negative charges determine the performance of IBFW (Supplementary Fig. S8).

When the HFIB cease to irradiate, the surface charges dissipate due to the drainage current and the electron-hole recombination (Fig. 2B) then the emitted cations induce the secondary anion emission. Both ions meet ahead of the CTL and form ion pairs. As a result, an ultra-thin precursor film with thickness comparable to ion size is formed at the irradiated area. At such thickness (Fig. 2C), the high disjoining pressure ($10^{5\sim6}$ Pa) irrigates and thickens the precursor film until balanced by the capillary force ($10^{2\sim3}$ Pa) and a continuous liquid film is formed.

The surface charging effect and the consequent ion emission is calculated and compared with experiment results (Fig. 2D). The surface charge density (SCD) of $SiO_2$ at HFIB irradiation [45–47] can be expressed as a function of time (Supplementary Note S2):

$$\frac{dQ(t)}{dt} = P(1+\gamma_e)\cdot I(t) - \frac{7}{4}\,Y\,I(t)\cdot\Omega_0\frac{Q(t)}{R_p} - \int_0^t J(t)dt - \sigma\frac{Q(t)}{\epsilon_r\epsilon_0}. \quad (1)$$

Where $P$ is the probability factor accounts for the electron-hole recombination; $\gamma_e$ is the secondary electron emission yield of $SiO_2$; $I(t)$ is the beam current; $Y$ is the sputtering yield; $\Omega_0$ is the atomic volume; $R_p$ is the ions stopping range; $J(t)$ is the IL ion emission rate; $\sigma$ is the substrate conductivity; $\epsilon_r$ is the substrate relative permittivity; and $\epsilon_0$ is the vacuum permittivity constant. The surface charge exerts electric field and distorts the IL-vacuum interface. When the interface distorted to be hemispherical, any increase of SCD ruptures the interface and induce significant ion emission[48–50]. The critical SCD depends on the distance between the starting scan spot and the reservoir CTL (Supplementary Note S3):

$$\sigma_{surf} \cong \frac{(d+r^*)^2+l_0(d+r^*)}{k_0 cos^3\alpha} E^*, \quad (2)$$

where $d$ is the distance between scan spot and the CTL, $r^* = \frac{q^6\gamma}{4\pi^2\epsilon_0^3(\Delta G)^4} \sim 10^{-8}m$ is the characteristic ion emission radius, $l_0$ is the surface charging area length scale, $\alpha$ is the ion emission angle, and $E^* \sim 10^{9\sim11}V/m$ is the characteristic electric field[49]. The blue line in Fig. 2B is the calculation results based on Eq. (2). The experimental SCD that takes to induce IBFW is calculated by Eq. (1) (orange squares in Fig. 2D) shows quadratic dependency on distance between starting scan spot and CTL. The calculation results agree well with the experimental results, and confirm our hypothesis that the surface charging induced ion emission accounts for the IBFW.

Apart from the HFIB configuration, the substrate characteristics also influence the IBFW behavior. As shown by Eq. (1), the electrical conductivity is easy to manipulate while exerts significant effect on the liquid inducing performance. In Fig. 2E, we select 7 different solid substrates vary from well conductor to dielectrics. The orange rectangles represent the lengths of liquid film that can be induced on different substrates under identical HFIB treatment. IL film cannot be induced on conductors such as Au and Cu, liquid extends slightly on semiconductor (Si), whereas liquid film propagates a long distance on insulated substrates *e.g.,* quartz and mica. Employing Eq. (1,2) and Supplementary Eq. (3.1), we can calculate the numbers of emitted ions during a single spot scan of HFIB (Supplementary Note S2, Fig. S9), and is depicted in Fig. 2E as blue circles. The qualitive consistency between the experimental and calculation results verifies the mechanism we propose. Molecular Dynamics simulation is employed to reveal the initiating stage of IBFW (Fig. 2G). The primary and secondary ion emissions are identified by the trajectories of cations and anions. We also observed an ultra-thin precursor film in MD simulation, see Supplementary Fig. S10.

We next verify that the disjoining pressure propels and stabilizes the nanofilm. The propagation speed of IBFW liquid film decreases monotonically with the increase of film length:

$$U \sim \frac{h^2}{3\mu} \cdot \frac{\Pi(h_{min})-\gamma\kappa}{L}. \quad (3)$$

Where $U$ is the average flow speed, $h$ is equilibrium film thickness, $\mu$ is IL viscosity, $\Pi(h_{min})$ is disjoining pressure at minimum film thickness $h_{min}$, $L$ is film length, $\gamma$ is IL surface tension, and $\kappa$ is curvature of IL-vacuum interface at the conjunction of film and reservoir (Supplementary Table. S2, Note S4, Fig. S11). The relationship between flow velocity and film length can also be measured experimentally (Supplementary Fig. S12). For comparison, we depict the calculation results as red line in Fig. 2F, and the red stars are the experimental results. The consistency suggests that disjoining pressure can explain the propagation of IBFW film. Besides, the equilibrium film thickness predicted by the balance between disjoining pressure[51,52] and Young-Laplace pressure agrees with the AFM measured average film thickness (Supplementary Note S5, Fig. S13). Hence, we prove that disjoining pressure is important in the propelling and stabilizing of IBFW nanofilm. Besides, we exclude the potential roles played by HFIB induced surface morphological or chemical modification effects and heating effect induced Marangoni flow in Supplementary Note S1 and more details of MD can be found in Supplementary Note S6.

**Working Performances and Application of IBFW**

We employ atomic force microscope (AFM) to manifest the nanoscale flow control of IBFW. Fig. 3A shows the front 7 $\mu m$ of a 28 $\mu m \times 1$ $\mu m$ IL film with thickness around 30~40 nm (an average of $35.4 \pm 1.7$ nm). The film thickness remains unchanged along the flow path (Fig.

3A). The film width is 1 μm, coincides with designed pattern. The liquid-vacuum interface is much smoother than solid substrate (RMS roughness $7.9 \pm 5.7$ nm). The minimal line width of IBFW film reaches $106\ nm$ (Supplementary Fig. S14), and is limited by the negative charge spatial distribution. If the negative surface charges can be trapped within a narrower spatial range, the ideal line width limitation may be comparable with film thickness.

The performances of IBFW are compared with published methods[23,24] in Fig. 3B-D. The IBFW film achieves a minimal line width and thickness which are two orders of magnitude lower than those induced by thermal and optical fields (Fig. 3B). Moreover, the IBFW prevents the formation of menisci between the film and the reservoir, which are common in previous studies where the corners between the film and the reservoir CTL usually have a radius of $20{\sim}40\ \mu m$. However, we achieve sharp corners (90°) with a corner radius of $20\ nm$ (Fig. 3C). IBFW also achieves relative high flow speed without substrate confinement. As shown in Fig. 3D, the flow speed is at least $2\ \mu m/s$ at $50\ \mu m$ film length with a 1 pA beam current, which is one order of magnitude higher than reported methods (lower than $0.5\ \mu m/s$).

The disjoining pressure harnessed in current work explains the better performances of IBFW. We delineate a system free energy ratio scenario for a liquid film system with unit length/ width and thickness vary from 1 nm to 4 mm in Fig. 3E, and the film thickness and corner radius are compared with published results[16,18,23,24]. System free energy composes of the volumetric term (gravity, electrostatic, *etc.*), the surface tension term, and the disjoining pressure term. The surface tension remains fixed magnitude of $10^1\ mN/m$, and its contribution to the system is almost constant with the thickness variation. When system size exceeds capillary length, $\lambda_{capillary}$, the volumetric term contributes most of the system free energy. At millimeter to micrometer range, the surface tension dominates, and the majority of traditional microfluidics methods belong to such region, with the spatial resolution difficult to approach nanoscale. When the system size reduces to nanometer region, the interfacial overlapping[31,33] emerges. The disjoining pressure increases rapidly when film thickness approaches sub-nanometer and dominates system energy. Following the capillary length, an overlapping length can be defined as $\lambda_{overlapping} \sim \sqrt{\frac{A_{slv}}{\gamma}} \sim 10^{-9\sim-8}\ m$, where $A_{slv}$ is the Hamaker constant of solid-liquid-vacuum interfaces system. Below such size the overlapping energy contribution far exceeds any other terms, and can be termed as the characteristic length scale for nanofluidics. Neither the traditional external stimuli or surface fabrication methods can acquire nanoscale control of flow, while the IBFW approaches the limit.

In Fig. 3F and Supplementary Fig. S18, we present a room-humidity-sensing circuit utilizing IBFW technique. The source-drain currents of a IBFW nanofilm circuit and a micrometer-size droplet circuit are measured within the same chamber with the relative humidity ranging from 40% to 70%. The current in nanofilm linearly depends on the humidity, while no significant change can be observed for micrometer droplet. The higher surface-volume ratio endowed by the nanometer thickness account for such differences. The results manifest the potential of IBFW in sensing circuit manufacture.

## Conclusion

In summary, we have demonstrated a novel strategy to control ionic liquid flow on dielectric substrates at nanoscale leveraging a novel IBFW mechanism. Distinct from the prevailing approaches, IBFW manipulates liquid film with minimal modification to both solid substrates and liquid. The performances of IBFW were manifested and are imparted by the utilizing of long-range intermolecular forces to stimulate and stabilize the nanofilm. IBFW can be

applied to fabricate rewritable liquid circuits with intricate desired patterns for sensing and reaction applications. Our findings will open a new avenue for versatile application fields such as on-demand manufacture of nano liquid circuit, in-situ combinational chemistry, efficient environmental gases sensing and adsorption.

## Methods

The fabrication details of the experiments used $SiO_2$ wafers are described below. An amorphous $SiO_2$ layer with a thickness of approximately 3 μm is deposited by plasma-enhanced chemical vapor deposition (PECVD) on a 500 μm thickness quartz substrate surface. Prior to the experiment, chips are cleaned with acetone, ethanol, and ultrapure water with ultrasonication. To remove any surface pollutants, the wafers are annealed in a tubing furnace at 320 ℃ with a mixture gas flow of hydrogen and argon for at least 3 hours.

The ionic liquids used in experiments are bought from Lanzhou Greenchem ILs, LICP, CAS. Prior to the experiment, the ionic liquid is dried in a vacuum at 80 ℃ for 24 h to remove the dissolved water.

A drop of ionic liquid (~ 100 μm diameter) is deposited by the capillary tube on the top surface of the SiO2 substrate acting as a liquid reservoir. Then, the sample is placed in a specimen holder in the vacuum chamber of a Zeiss helium ion microscope. The images are secondary electron images acquired by the raster scans of 30 kV He focused ion beam.

The proof-of-concept and the rewritable tests of IBFW technology employed one single PECVD $SiO_2$ wafer with preparation procedures discussed previously and a micro droplet of [EMIM][DCA] ionic liquid was deposited on the silica wafer repeatedly. After sample preparation, the solid substrate with liquid reservoir settled on the top is transferred into the HIM chamber. The CTL of droplet reservoir is identified under imaging mode, and NPVE software is employed to fabricate a $20\ \mu m \times 1\ \mu m$ film pattern with the flood gun turned on to guarantee the fabricated film reproduces the pattern (the reason is discussed in Fig. S8). After IBFW fabrication, the sample is transferred and the film pattern is characterized under the tapping mode of AFM. Once characterization is done, the solid substrate is merged into a beaker filled with acetone and placed inside a fume cupboard for 24h. After dissolving the IL droplet and film with acetone, an ultrasonic cleaner and deionized water are employed to eliminate the residual acetone of the substrate. Such procedures were repeated for ten times in the rewritable tests.

The molecular dynamics simulation details can be found in Supplementary Note S6.

The IL nanofilm circuit for gas sensing is fabricated as follow. Electrodes (Ti/Au, 5/50 nm) are deposited on doped Si wafer covered with 300 nm of $SiO_2$ by means of lithography, electron beam evaporation, and lift off procedure. Two droplets of [EMIM][DCA] IL with radius ~250 μm are deposited on the electrodes acting as the liquid reservoirs. IL film connecting two reservoirs on the electrodes is obtained by the IBFW method to construct a circuit with 0.5 μm width and 80 μm length. The optical image of the device is shown in Fig. S18B. All the transient measurements were performed at room temperature (25 °C) employing a Keithley Sourcemeter2636B, biased with a constant voltage between the source and drain electrodes.

**References and Notes**


1. Dai, H., Dong, Z. & Jiang, L. Directional liquid dynamics of interfaces with superwettability. *Sci. Adv.* **6**, eabb5528 (2020).
2. Liu, M., Wang, S. & Jiang, L. Nature-inspired superwettability systems. *Nat. Rev. Mater.* **2**, 1–17 (2017).
3. Lee, W. *et al.* Universal assembly of liquid metal particles in polymers enables elastic printed circuit board. *Science* **378**, 637–641 (2022).
4. Ferraro, P., Coppola, S., Grilli, S., Paturzo, M. & Vespini, V. Dispensing nano–pico droplets and liquid patterning by pyroelectrodynamic shooting. *Nat. Nanotechnol.* **5**, 429–435 (2010).
5. Hou, X. *et al.* Interplay between materials and microfluidics. *Nat. Rev. Mater.* **2**, 1–15 (2017).
6. Frey, N., Sönmez, U. M., Minden, J. & LeDuc, P. Microfluidics for understanding model organisms. *Nat. Commun.* **13**, 3195 (2022).
7. Xu, W. *et al.* A droplet-based electricity generator with high instantaneous power density. *Nature* **578**, 392–396 (2020).
8. Zhang, C. *et al.* Superaerophilic/superaerophobic cooperative electrode for efficient hydrogen evolution reaction via enhanced mass transfer. *Sci. Adv.* **9**, eadd6978 (2023).
9. Kim, H. *et al.* Water harvesting from air with metal-organic frameworks powered by natural sunlight. *Science* **356**, 430–434 (2017).
10. Yang, Z., Wei, J., Sobolev, Y. I. & Grzybowski, B. A. Systems of mechanized and reactive droplets powered by multi-responsive surfactants. *Nature* **553**, 313–318 (2018).
11. Chen, H. *et al.* Ultrafast water harvesting and transport in hierarchical microchannels. *Nat. Mater.* **17**, 935–942 (2018).
12. Yu, T. *et al.* Microchannels with Self-Pumping Walls. *ACS Nano* **14**, 13673–13680 (2020).

13. Feng, S. *et al.* Three-dimensional capillary ratchet-induced liquid directional steering. *Science* **373**, 1344–1348 (2021).
14. Chen, H. *et al.* Continuous directional water transport on the peristome surface of Nepenthes alata. *Nature* **532**, 85–89 (2016).
15. Wong, T.-S. *et al.* Bioinspired self-repairing slippery surfaces with pressure-stable omniphobicity. *Nature* **477**, 443–447 (2011).
16. Zheng, Y. *et al.* Directional water collection on wetted spider silk. *Nature* **463**, 640–643 (2010).
17. Chu, K.-H., Xiao, R. & Wang, E. N. Uni-directional liquid spreading on asymmetric nanostructured surfaces. *Nat. Mater.* **9**, 413–417 (2010).
18. Prakash, M., Quéré, D. & Bush, J. W. M. Surface Tension Transport of Prey by Feeding Shorebirds: The Capillary Ratchet. *Science* **320**, 931–934 (2008).
19. Gao, X. & Jiang, L. Water-repellent legs of water striders. *Nature* **432**, 36–36 (2004).
20. Park, K.-C. *et al.* Condensation on slippery asymmetric bumps. *Nature* **531**, 78–82 (2016).
21. Chaudhury, M. K. & Whitesides, G. M. How to Make Water Run Uphill. *Science* **256**, 1539–1541 (1992).
22. Xu, Y. *et al.* Liquid crystal–based open surface microfluidics manipulate liquid mobility and chemical composition on demand. *Sci. Adv.* **7**, eabi7607 (2021).
23. Kataoka, D. E. & Troian, S. M. Patterning liquid flow on the microscopic scale. *Nature* **402**, 794–797 (1999).
24. Garnier, N., Grigoriev, R. O. & Schatz, M. F. Optical Manipulation of Microscale Fluid Flow. *Phys. Rev. Lett.* **91**, 054501 (2003).
25. Liu, G. L., Kim, J., Lu, Y. & Lee, L. P. Optofluidic control using photothermal nanoparticles. *Nat. Mater.* **5**, 27–32 (2006).

26. Li, A. *et al.* Programmable droplet manipulation by a magnetic-actuated robot. *Sci. Adv.* **6**, eaay5808 (2020).

27. Dunne, P. *et al.* Liquid flow and control without solid walls. *Nature* **581**, 58–62 (2020).

28. Han, X., Tan, S., Jin, R., Jiang, L. & Heng, L. Noncontact Charge Shielding Knife for Liquid Microfluidics. *J. Am. Chem. Soc.* (2023) doi:10.1021/jacs.2c13674.

29. Jin, Y. *et al.* Electrostatic tweezer for droplet manipulation. *Proc. Natl. Acad. Sci.* **119**, e2105459119 (2022).

30. Cazabat, A. M., Heslot, F., Troian, S. M. & Carles, P. Fingering instability of thin spreading films driven by temperature gradients. *Nature* **346**, 824–826 (1990).

31. Dong, W. Nanoscale thermodynamics needs the concept of a disjoining chemical potential. *Nat. Commun.* **14**, 1824 (2023).

32. Stewart, M. C. & Evans, R. Layering transitions and solvation forces in an asymmetrically confined fluid. *J. Chem. Phys.* **140**, 134704 (2014).

33. Derjaguin, B. V., Rabinovich, Y. I. & Churaev, N. V. Measurement of forces of molecular attraction of crossed fibres as a function of width of air gap. *Nature* **265**, 520–521 (1977).

34. Oron, A., Davis, S. H. & Bankoff, S. G. Long-scale evolution of thin liquid films. *Rev. Mod. Phys.* **69**, 931–980 (1997).

35. Kleinert, J., Kim, S. & Velev, O. D. Electric-Field-Controlled Flow in Nanoscale-Thin Wetting Films. *Langmuir* **28**, 3037–3044 (2012).

36. Deng, Y., Chen, L., Liu, Q., Yu, J. & Wang, H. Nanoscale View of Dewetting and Coating on Partially Wetted Solids. *J. Phys. Chem. Lett.* **7**, 1763–1768 (2016).

37. Sun, Q. *et al.* Surface charge printing for programmed droplet transport. *Nat. Mater.* **18**, 936–941 (2019).

38. Shen, P.-C. *et al.* Ultralow contact resistance between semimetal and monolayer semiconductors. *Nature* **593**, 211–217 (2021).

39. Mirsaidov, U. M., Zheng, H., Bhattacharya, D., Casana, Y. & Matsudaira, P. Direct observation of stick-slip movements of water nanodroplets induced by an electron beam. *Proc. Natl. Acad. Sci.* **109**, 7187–7190 (2012).

40. Uddin, S. *et al.* Lipid based biocompatible ionic liquids: synthesis, characterization and biocompatibility evaluation. *Chem. Commun. Camb. Engl.* **56**, 13756–13759 (2020).

41. Kumar, A., Bisht, M. & Venkatesu, P. Biocompatibility of ionic liquids towards protein stability: A comprehensive overview on the current understanding and their implications. *Int. J. Biol. Macromol.* **96**, 611–651 (2017).

42. Huang, C., Li, J. & Li, M. Performance measurement and evaluation of an ionic liquid electrospray thruster. *Chin. J. Aeronaut.* **36**, (2021).

43. Zhang, Y., Ye, J., Matsuhashi, Y. & Iwasa, Y. Ambipolar MoS2 Thin Flake Transistors. *Nano Lett.* **12**, 1136–1140 (2012).

44. Ohya, K. & Yamanaka, T. Modeling secondary electron emission from nanostructured materials in helium ion microscope. *Nucl. Instrum. Methods Phys. Res. Sect. B Beam Interact. Mater. At.* **315**, 295–299 (2013).

45. Ishitani, T., Yamanaka, T., Inai, K. & Ohya, K. Secondary electron emission in scanning Ga ion, He ion and electron microscopes. *Vacuum* **84**, 1018–1024 (2010).

46. Yogev, S. *et al.* Charging of dielectrics under focused ion beam irradiation. *J. Appl. Phys.* **103**, 064107 (2008).

47. Lenahan, P. M., Mele, J. J., Lowry, R. K. & Woodbury, D. Leakage currents and silicon dangling bonds in amorphous silicon dioxide thin films. *J. Non-Cryst. Solids* **266–269**, 835–839 (2000).

48. Iribarne, J. V. & Thomson, B. A. On the evaporation of small ions from charged droplets. *J. Chem. Phys.* **64**, 2287–2294 (1976).

49. Zhang, F. *et al.* Electric-Field-Driven Ion Emission from the Free Surface of Room Temperature Ionic Liquids. *J. Phys. Chem. Lett.* **12**, 711–716 (2021).

50. Coffman, C. S., Martínez-Sánchez, M. & Lozano, P. C. Electrohydrodynamics of an ionic liquid meniscus during evaporation of ions in a regime of high electric field. *Phys. Rev. E* **99**, 063108 (2019).

51. London, F. Zur Theorie und Systematik der Molekularkräfte. *Z. Für Phys.* **63**, 245–279 (1930).

52. Bhatt, B., Gupta, S., Sumathi, V., Chandran, S. & Khare, K. Electric Field Driven Reversible Spinodal Dewetting of Thin Liquid Films on Slippery Surfaces. *Adv. Mater. Interfaces* 2202063 (2023).

53. Stukowski, A. Visualization and analysis of atomistic simulation data with OVITO–the Open Visualization Tool. *Model. Simul. Mater. Sci. Eng.* **18**, 015012 (2009).

54. Canongia Lopes, J. N., Pádua, A. A. H. & Shimizu, K. Molecular Force Field for Ionic Liquids IV: Trialkylimidazolium and Alkoxycarbonyl-Imidazolium Cations; Alkylsulfonate and Alkylsulfate Anions. *J. Phys. Chem. B* **112**, 5039–5046 (2008).

55. Canongia Lopes, J. N. & Pádua, A. A. H. Molecular Force Field for Ionic Liquids III: Imidazolium, Pyridinium, and Phosphonium Cations; Chloride, Bromide, and Dicyanamide Anions. *J. Phys. Chem. B* **110**, 19586–19592 (2006).

56. Canongia Lopes, J. N. & Pádua, A. A. H. Molecular Force Field for Ionic Liquids Composed of Triflate or Bistriflylimide Anions. *J. Phys. Chem. B* **108**, 16893–16898 (2004).

57. Jorgensen, W. L., Maxwell, D. S. & Tirado-Rives, J. Development and Testing of the OPLS All-Atom Force Field on Conformational Energetics and Properties of Organic Liquids. *J. Am. Chem. Soc.* **118**, 11225–11236 (1996).
58. Martínez, L., Andrade, R., Birgin, E. G. & Martínez, J. M. PACKMOL: A package for building initial configurations for molecular dynamics simulations. *J. Comput. Chem.* **30**, 2157–2164 (2009).
59. Canongia Lopes, J. N., Deschamps, J. & Pádua, A. A. H. Modeling Ionic Liquids Using a Systematic All-Atom Force Field. *J. Phys. Chem. B* **108**, 2038–2047 (2004).
60. Klomfar, J., Součková, M. & Pátek, J. Temperature Dependence of the Surface Tension and Density at 0.1 MPa for 1-Ethyl- and 1-Butyl-3-methylimidazolium Dicyanamide. *J. Chem. Eng. Data* **56**, 3454–3462 (2011).
61. Li, Y. *et al.* Ultrafast Diameter-Dependent Water Evaporation from Nanopores. *ACS Nano* **13**, 3363–3372 (2019).
62. Penkov, O. V. *et al.* Ion-beam irradiation of DLC-based nanocomposite: Creation of a highly biocompatible surface. *Appl. Surf. Sci.* **469**, 896–903 (2019).
63. Chen, Y., Zhao, Z. & Liu, Y. Wettability characteristic of PTFE and glass surface irradiated by keV ions. *Appl. Surf. Sci.* **254**, 5497–5500 (2008).
64. Ziegler, J. F., Ziegler, M. D. & Biersack, J. P. SRIM – The stopping and range of ions in matter (2010). *Nucl. Instrum. Methods Phys. Res. Sect. B Beam Interact. Mater. At.* **268**, 1818–1823 (2010).
65. Fox, D. *et al.* Helium ion microscopy of graphene: beam damage, image quality and edge contrast. *Nanotechnology* **24**, 335702 (2013).

**Acknowledgments:**

**Funding:**

This work was supported by National Natural Science Foundation of China (No. 51976001).

**Author contributions:**

H.G., K.M., R.Y., H.W. conceived and designed the experiments. H.W. and R.Z. supervised the study and experiments. H.G. and K.M. analyzed the experiment results and proposed the theoretical models. H.G. conducted the MD simulation and data process coding. S.X. and C.D. fabricated and provided the silica substrates. X.L. conducted the electrical probe testing. R.L. and L.L. conducted the vacuum electrical probe testing. Y.S. helped with the surface annealing of the $SiO_2$ substrate. Y.D. helped with the measurements of IL contact angle. X.W. conducted the lithography fabrication of the circuit. H.G. and K.M. wrote the original draft. K.M., H.W.,C.D., R.Y. and Y.D. revised the manuscript. All the authors discussed the results and provided comments.

**Competing interests:** Authors declare that they have no competing interests.

**Data and materials availability:** All data are available in the main text or the supplementary materials. Any requisition for code and technique detail should address to the corresponding author.

**Supplementary Materials**

Supplementary Text

Tables S1 to S3

Notes S1 to S6

Figs. S1 to S18

Video. S1 to S4

References (*53–65*)

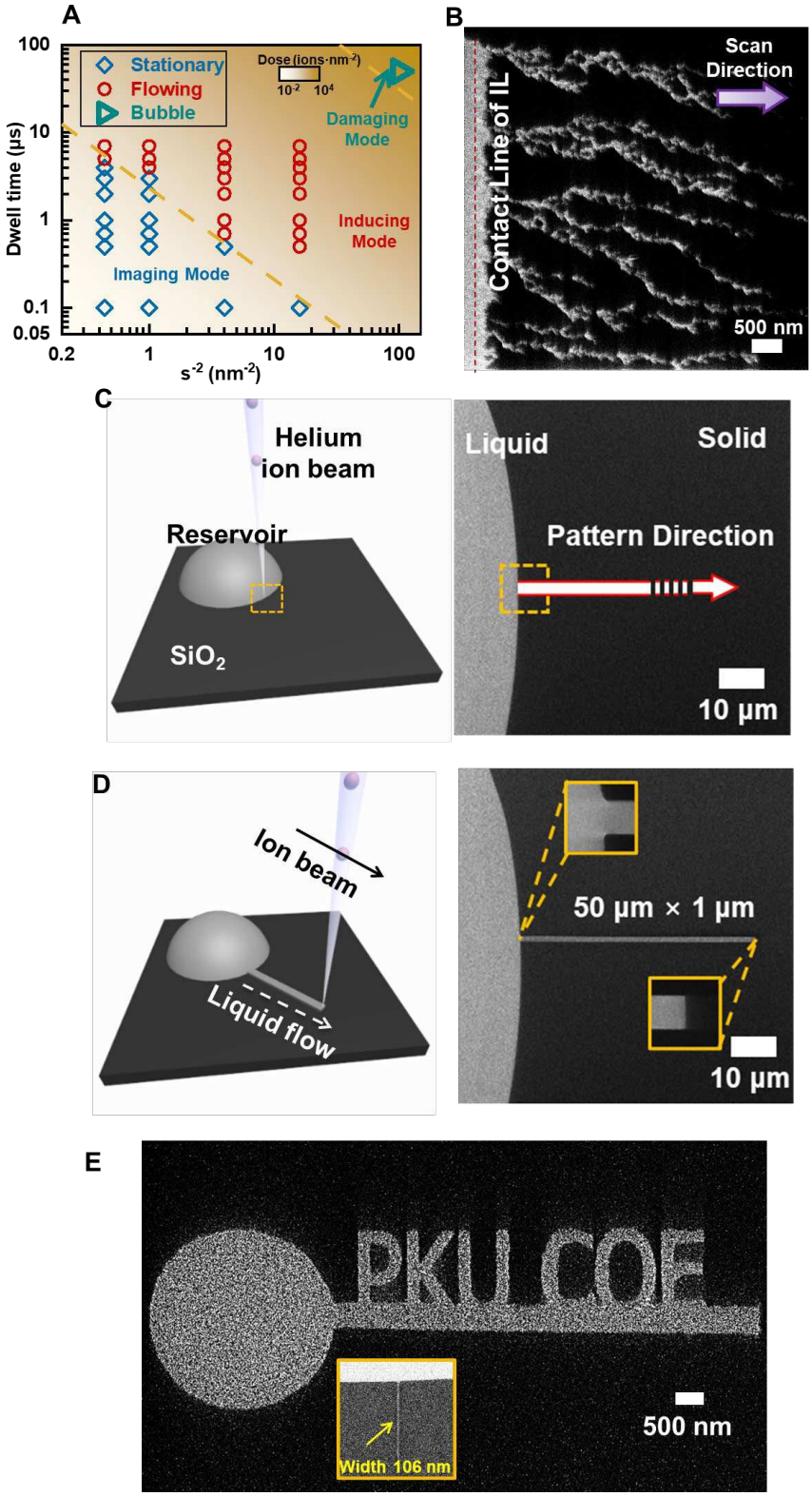


**Fig. 1. HFIB liquid inducing mode and working procedure of IBFW nano-printing.** (**A**) A phase diagram of three working modes under different HFIB dose, manipulated by the dwell and the scan spot density. The background color map shows the dose density ranges from $10^{-2}\sim10^{4} ions/nm^2$. The imaging mode exerts no influence to samples (blue squares); the

inducing mode can induce directional liquid flow (red circles); and the damaging mode can etch samples and induce Helium bubbling (cyan triangle). (**B**) The hierarchical branched flow pattern of IL after a frame of HFIB scan. The IL will eventually fill the entire irradiated area in 30 s. (**C**) CTL region of the IL reservoir and NPVE pattern design. Left is a schematic, and right is an HIM image. The white arrow indicates the pattern direction and area in NPVE. (**D**) The rectangular film pattern (50 μm×1 μm) fabricated by IBFW. The insets are the details to manifest small corner radius and well reproduction of the design. (**E**) The IBFW fabricated 'PKU COE' pattern and demonstrate its potential in on-demand printing of complex liquid film networks. The inset shows an example of the minimal line width pattern that IBFW can fabricate.

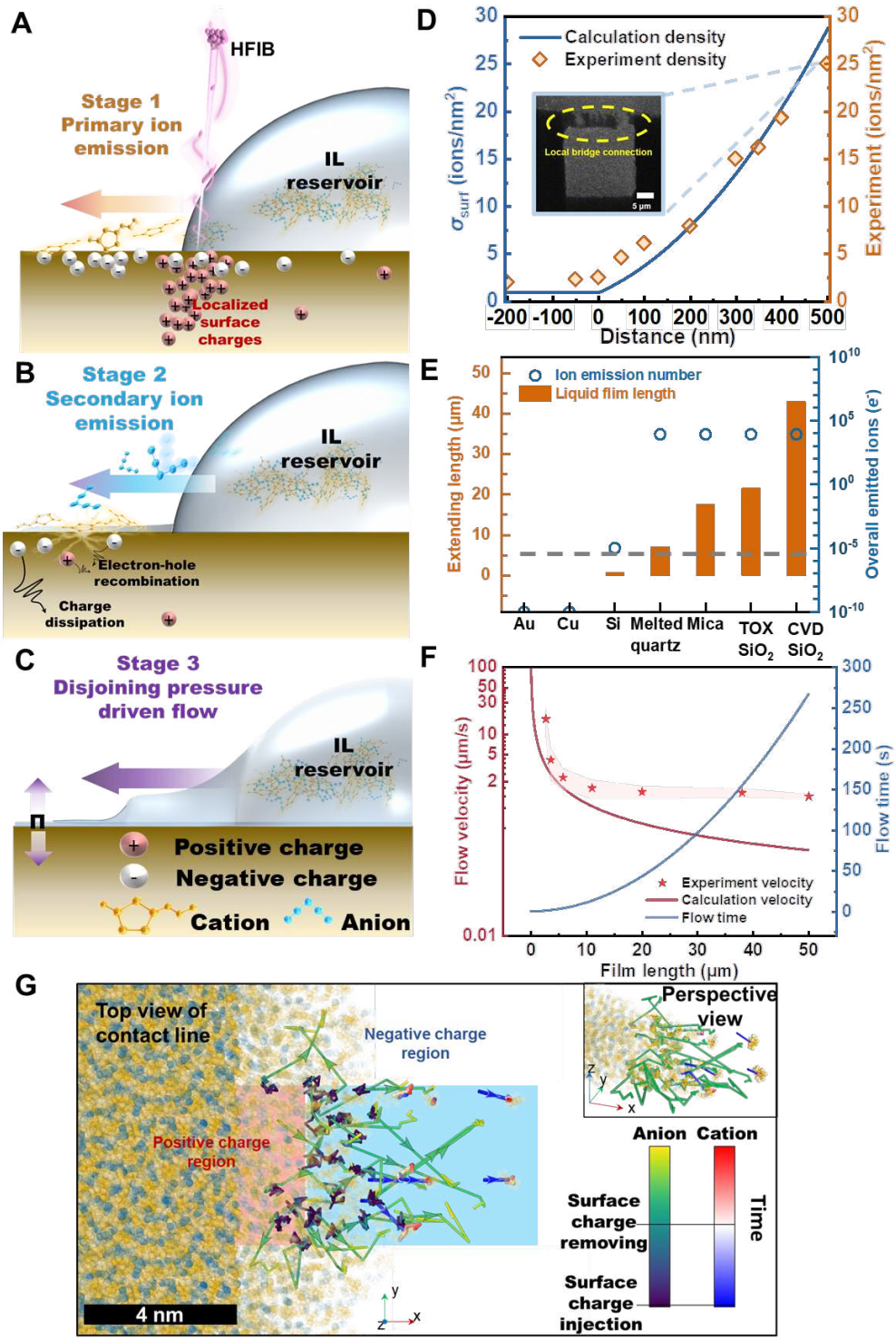


**Fig. 2. Working principle of IBFW nano-printing.** (**A-C**) Schematic of the IBFW working principle. (**A**) When HFIB irradiates the CTL, the negative surface charging induces the primary cation emission. (**B**) When HFIB ceases to scan, surface charging dissipates and the emitted cations induce the secondary anion emission. (**C**) The emitted ions from previous stages form a ultra-thin precursor film, and the consequent disjoining pressure propels and stabilizes liquid film. (**D**) Experimentally characterized surface charge density to induce IL flow (ions per square

of nm) and calculation results. The inset shows when the scan position is separated too far from the CTL, the consecutive liquid film degenerates to the local protrusion flow as shown in Fig. 1B. (**E**) IBFW induced liquid film lengths (μm) on substrates with different conductivities. The right ordinate represents the overall ion emission number calculated by the beam parameters and sample characters. (**F**) IBFW film flow speed as a function of liquid film length. The shaded region represents error based on uncertainties of the frame scan speed of HIM. The predicted results of average flow speed and the time it takes to irrigate the pattern are also included. (**G**) Molecular dynamics simulation of [EMIM][DCA] droplet (640 ion pairs) deposited on fused silica substrate going through surface charges injection and removement. The arrows indicate the most directed movements of ions: the blue arrows at the beginning stage represent the surface charge induced primary cation emission; the green to yellow arrows of anions represent the emitted cations induced secondary anion emission. The shaded regions (red and blue) represent the surface injection area for positive and negative respectively.

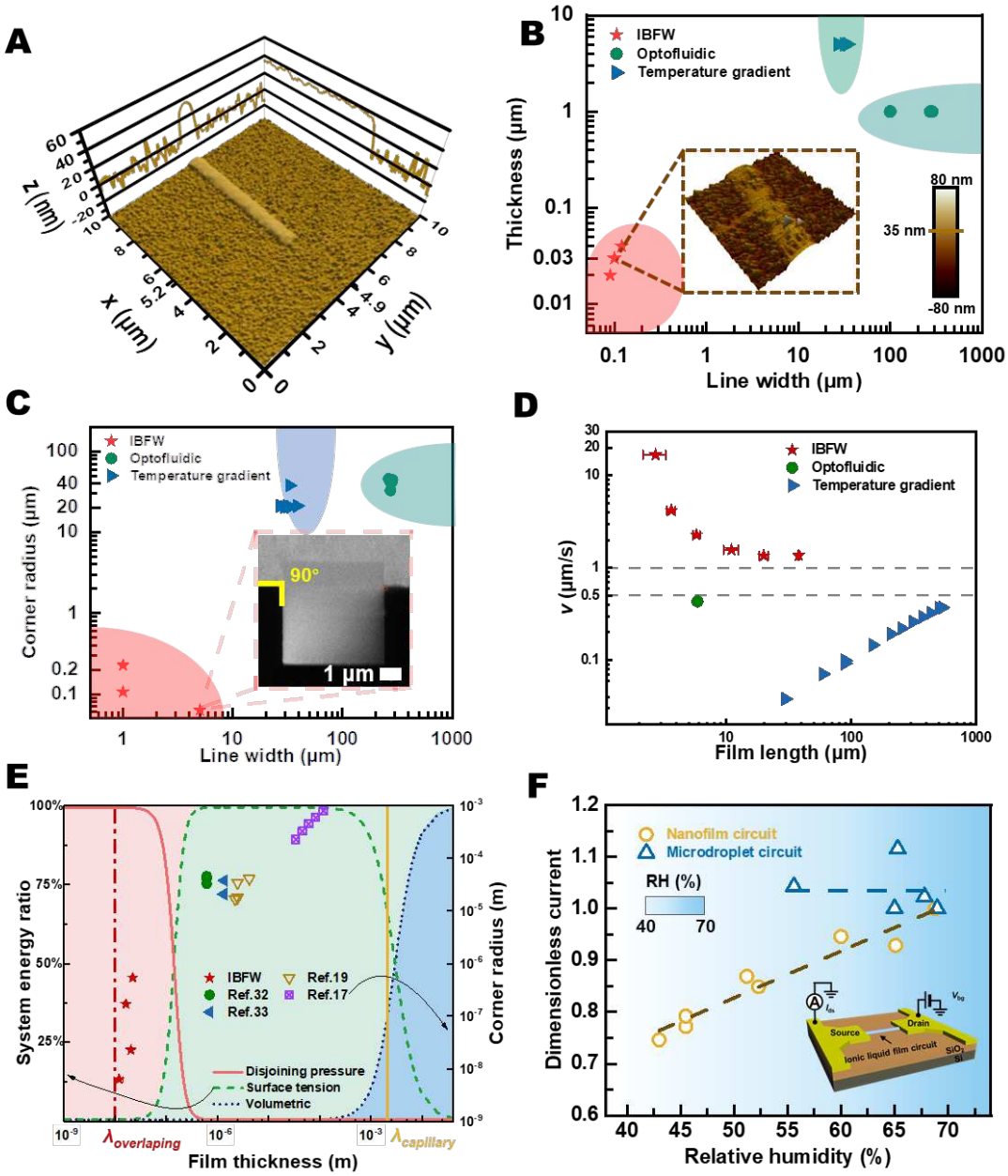


**Fig. 3. Working performances and application of IBFW.** (**A**) Tapping mode AFM image of the front 7 μm of a 28 μm×1 μm IL film. (**B**) The liquid film line width and thickness compared with published results[23,24]. The inset show part of the IBFW liquid film imaged by AFM. The corner radiuses between the fabricated liquid film and reservoir are compared in (**C**) with the inset illustrate a IBFW film with corner radius down to 20 nm, and flow velocities at different liquid film lengths are illustrated in (**D**). The shaded areas in (B) and (C) indicate the flow control regions that different methods fall in. (**E**) System free energy scenario of a liquid film with different flow control strategies. The left ordinate represents the ratio that different energy terms contribute to the total free energy, and shaded regions (blue, green and red) represents the volumetric force dominates macroscale system (blue), surface tension dominates micrometer system (green) and disjoining pressure dominates nanometer system (red). The red yellow vertical line represents capillary length and the red represents overlapping length

($\lambda_{overlapping} \sim \sqrt{\frac{A_{slv}}{\gamma}}$) Different symbols represent different strategies, the IBFW push the limit towards nanoscale while most counterparts fall in the surface tension region. (**F**) Proof-of-concept gas sensing prototype. The inset shows the schematic of a room-humidity sensor based on IBFW fabricated nanofilm. The drainage-source currents of both microdroplet and nanofilm are illustrated and the linear fitting results are depicted as dash lines. The background color map represents the relative humidity of test chamber ranges from 40% to 70%.

## Supplementary Files

This is a list of supplementary files associated with this preprint. Click to download.

- NCSupplementarymaterials.pdf
- SupplementaryVideo1.mp4
- SupplementaryVideo2.mp4
- SupplementaryVideo3.mp4
- SupplementaryVideo4.mp4